Inverse Problems **25** (2009) 024001 (18pp) doi:10.1088/0266-5611/25/2/024001

Continuing with the Fresnel database: experimental setup and improvements in 3D scattering measurements

J M Geffrin and P Sabouroux

Institut Fresnel, Aix-Marseille Université, Ecole Centrale Marseille, CNRS, Domaine Universitaire de Saint Jérôme, 13397 Marseille, France

E-mail: jean-michel.geffrin@fresnel.fr

Received 7 July 2008, in final form 7 November 2008
Published 6 February 2009
Online at stacks.iop.org/IP/25/024001

Abstract

In this paper, the experimental setup and the improvements required to obtain further measurements for the third opus of the Fresnel Database are presented. The most original feature of those new datasets is the fact that they were obtained with three-dimensional targets instead of the two-dimensional ones used in the two previous opuses. The measurements were performed all around the targets under test to collect enough information about the objects to be able to perform inversion on their scattered fields. As the targets were small in comparison with the wavelength, the challenge here was to extract these small scattered fields from the measurements, and a specific post-processing procedure had to be designed to compensate for the drift errors. The five targets selected for the database are presented, including the *Myster* target, a hitherto undivulged target that is presented in this paper for the first time, i.e., at the same time as the submissions of all the other contributors to this special section. Some scattered field comparisons are also presented.

(Some figures in this article are in colour only in the electronic version)

1. Introduction

Continuing our project to provide the inversion community with useful experimental data, which was inspired by the Ipswitch database [1–4], a third Fresnel Database opus has been created. The most novel feature of this opus is the fact that it now contains experimental scattering data obtained with three-dimensional targets instead of the two-dimensional ones previously investigated. Our aim is still to enable investigators to test and validate their inversion algorithms by confronting them with a set of data on electromagnetic scattered fields which have been measured experimentally in a controlled environment.

In the first opus of the Fresnel Database, in the special section of the *Inverse Problems* journal 'Testing inversion algorithms against experimental data' [5], preliminary results were reported in 11 contributions from several research teams. Homogeneous targets were measured in a multi-frequency, multi-static configuration and the experimental data can be downloaded freely for scientific use. A detailed description of the measurement configuration specific to this opus can be found in [5].

In the second opus, in response to the comments made by several colleagues, another dataset was provided on inhomogeneous targets measured in both transverse electric and transverse magnetic polarization. This dataset corresponds to the second special section of the *Inverse Problems* journal entitled 'Testing inversion algorithms against experimental data: inhomogeneous targets' [6]. Again, 11 contributions from several research teams were presented. A large range of inversion scattering techniques were used successfully here to reconstruct the profiles of the inhomogeneous objects studied. The experimental data obtained can again be freely downloaded for scientific use. A detailed description of the measurement configuration specific to this opus can be found in [7].

In the present opus, considerable time and effort have been devoted to measuring the fields scattered by three-dimensional (3D) targets so that they can be used for inversion purposes. The challenges arising here were due to the very low level of the signal of interest (the scattered field) in comparison with the signals measured (the total and incident fields) when the size of the targets is smaller than the wavelength: a trade off was required in this case to render inversions possible. The scattered field measured on the receivers can typically be 25 dB lower than the incident field level. In addition, as measurements in the equatorial plane alone do not provide sufficient information, the source had to be moved elsewhere, and this resulted in a much longer acquisition time. As far as we know, there exist few types of equipment which are suitable for this purpose, and even less data are available on this topic (see [10] for measurements at a single frequency). The few other measured data available in the literature focused more on radar imaging. The high level of accuracy required for inversion purposes has also led to several improvements being made to the measurement system itself as well as to the data processing.

This paper is organized as follows. In section 2, the experimental setup used to perform the measurements is briefly recalled and the modifications introduced since the previous Fresnel Database opus are described. The method used for the post-processing of the data measured is then described in detail in section 3, especially the drift correction procedure based on the *a priori* knowledge of the spectral bandwidth of the scattered field. The five targets, including the *Myster* target, which has been kept secret from all the other contributors up to now, are then presented in section 4. Section 5 is devoted to presenting the data file format. Section 6 makes some scattered field comparisons between measured and simulated fields, as well as presenting some plots showing the effects of the drift correction. Lastly, in section 7, some conclusions are drawn.

2. Experimental setup description

2.1. Anechoic chamber, positioning devices, and network analyzer

The present experiments were carried out in the anechoic chamber of the *Centre Commun de Ressources Micro-Ondes* (CCRM), which was adapted for this purpose by members of the Institut Fresnel. This anechoic chamber is the largest microwave measurement setup developed at our laboratory.

Figure 1. Picture of the anechoic chamber at the CCRM which was used to measure the scattered field data presented in the database.

This system has been previously described in several papers, the most recent of which was [9]. This anechoic chamber is enclosed in a large Faradized cage 14.50 m long, 6.50 m wide and 6.50 m high, which makes it possible to simply model all the propagation processes as free space processes, which facilitates the modeling of the forward problem. The main specificity of this equipment is the semi-circular vertical arch, through which two wagons are able to move along almost a whole meridian (figure 1). Contrary to the 2D target measurements, it was necessary in this case to be able to place the source outside the azimuthal plane in order to obtain enough information about the target under investigation. Our equipment was designed for studying a large range of experimental configurations, thanks to the five mechanical positioning devices it comprised. The first positioning device serves to adjust the orientation of the target at the center of the setup. As the targets chosen are not too heavy, each of them was placed on an expanded polystyrene mast. The second positioning device controls the receiving antenna, which is placed on an arm rotating around the vertical axis within the azimuthal plane. The third and fourth devices control the displacement of the two wagons supporting the source(s) antenna(s) through the semi-circular arch. Both the azimuthal arm and the arch have a radius of about 2 m. The fifth positioning device, which was not used in the present scattering measurements, is placed 10.5 m from the target and is used to perform radar cross section (RCS) measurements.

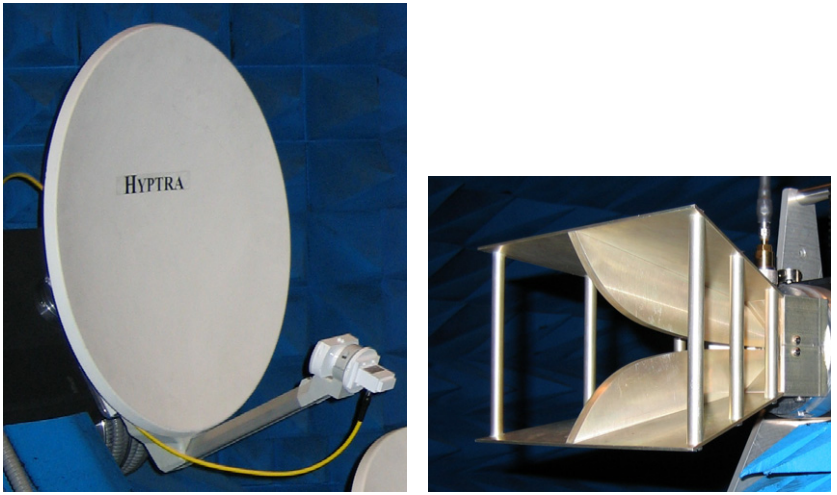

Figure 2. Transmitting (left) and receiving (right) antennas used to acquire the scattered fields in the anechoic chamber.

This setup operates in the 300 MHz–26.5 GHz frequency range. All the present measurements were performed with a vector network analyzer (Agilent HP 8510), which was used in a multiple sources configuration with two synthesizers and two external mixers (the measured noise floor level is about −100 dB and the dynamic range is between 70 and 100 dB, depending on the frequency). All the mechanical movements and the network analyzer are controlled and synchronized by a PC and a C++ monitoring program. As previously, the scattered field was not measured directly but obtained by subtracting the incident field from the total field, both of which were measured on the receivers. Based on previous experience, the incident field and the total field were both measured in the same direction (clockwise or counter clockwise) to prevent positioning uncertainties.

2.2. Transmitting and receiving antennas

Another difference with the 2D scattering measurements was the fact that the source antenna had to be replaced by a parabolic antenna to obtain a reasonable signal level, but this reduced the possible frequency band. The transmitting antennas used are parabolic antennas with a frequency range of 3–8 GHz. As the targets are very small (they are generally even less than a wavelength in size at the lower frequencies), we had to focus the radiated energy onto the targets in order to increase the scattered field level. This choice of rather small targets was in fact due to the possibilities of 3D inversion algorithms, which are often not compatible with investigation domains more than a few cubic wavelengths in size. These parabolic antennas (Hyptra NE5256, figure 2(a)) give quite a good compromise between the working frequency band and the directivity. The receiving antenna is a ridged horn antenna (ARA DRG 118A, figure 2(b)) as in the previous opuses. Both antennas are linearly polarized and the different polarizations are obtained by rotating the antennas.

As can be seen from figure 1, two identical parabolas were used here with a hyperfrequency switch in order to reduce the acquisition time. This option has some drawbacks, because in order to switch between the two antennas, the mixer has to be placed before the switch, which means keeping 9 m of high-frequency cables between the reference mixer and the

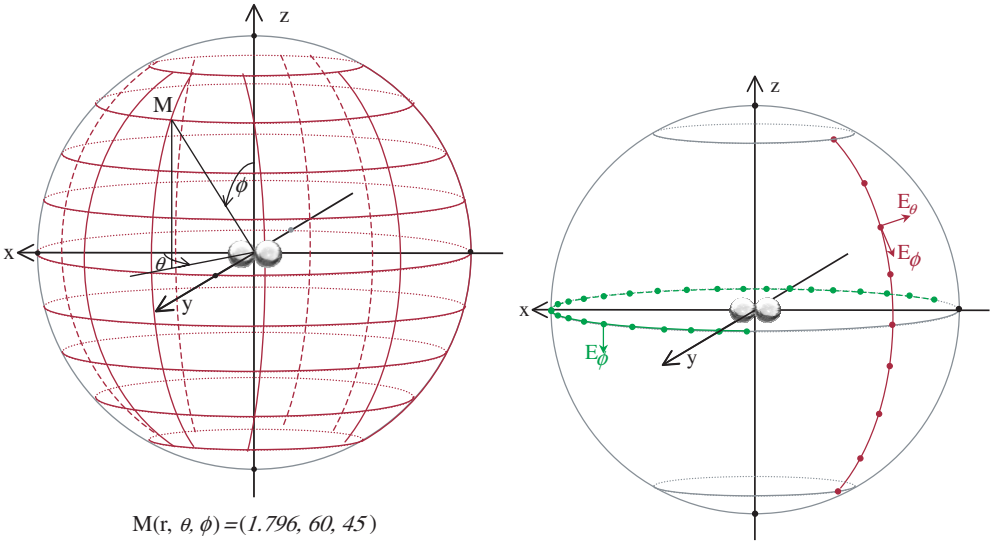

Figure 3. Position of the sources (left) and the receivers (right) on the measurement sphere, and definition of the angles and polarizations.

antenna. When external mixers are used, the objective is usually to keep this length as short as possible to avoid losses and problems due to bent cables or temperature variations [11], but the configuration adopted has in fact been validated (see [9]). Another requirement when making these measurements with two sources is that it must be possible to reconnect the two hemispheres together. This was done by comparing the fields obtained in the equatorial plane, where the total field and incident field were measured with the two parabolas.

One key issue when dealing with inverse problems is that it is necessary to ensure that the scattered field contains a sufficient amount of information about the target. Since the targets under investigation here are three-dimensional ones, many more measurements are necessary than in the two-dimensional case, and the source therefore has to be moved out of the azimuthal plane; two polarizations also have to be used. As established in [12], the requisite amount of information can be obtained when the minimum sphere including the target is known. For practical reasons, the additional constraint consisting in keeping the total measurement time to less than 24 h was adopted, and thus the ideal criterion could not always be satisfied with every target and every frequency. Given the possibilities of our equipment, the following parameters were chosen.

2.3. Sources locations

The sources were located all round the target, $r = 1.796$ m from the center (assuming a reference frame to be applied to the target). The azimuthal angle θ_s ranged from 20° to 340° with a 40° step (i.e., 9 meridians) and the polar angle ϕ_s ranged from 30° to 150° with a 15° step (i.e., there were 9 parallels) (figure 3). This angular convention is commonly used in Mathematics.

As the source antennas were parabolas, the incident field could be taken to be a plane wave within the whole volume containing the target. All measurements were made at 21 frequencies ranging from 3 to 8 GHz with a 0.25 GHz step. The lower frequencies have to

be handled carefully because they correspond to the lowest frequencies at which the parabolas can be used. At these frequencies, the targets are therefore very small in comparison with the wavelength, and their scattered fields are also quite small and not readily distinguishable from the background noise (especially with the cross polarization).

2.4. Receiver locations

Due to the design of our system, the receivers are restricted to the azimuthal plane (i.e., $\phi = 90°$) at $r = 1.796$ m from the center and for technical reasons, they cannot be closer to the source meridian than 50°. The azimuthal angle θ_r therefore ranged from 0 to 350° with a 10° step, but there are some exclusions (figure 3). Note that this step was much larger than those used previously, but this is now possible because of the drift corrections applied (see section 3.1). Some other receiver positions were ruled out due to the saturation of the mixer placed behind the receiving antenna [13]: the highest field amplitudes are measured when the receiver is placed in front of the transmitting antenna. To optimize our measurements inside the available dynamic range, a compromise had to be made between the low levels available and the saturation. We preferred to ensure a high level of accuracy at these low levels rather than keeping the entire main scattering lobe by lowering the synthesizer power. Some measurements made in front of the source when saturation was reached have therefore been removed from the data files (and have been replaced by zero scattered field values).

2.5. Antenna polarizations

Two polarization cases are measured (figure 3):

- source polarized along E_ϕ and receiver polarized along E_ϕ,
- source polarized along E_θ and receiver polarized along E_ϕ.

Note that reciprocity can also be used by reversing the roles of the source and receiver, if a single polarization is preferred for the incident wave, as done in [14].

3. Post-processing the measured fields

To obtain suitable scattered field measurements with these low scattering targets, we are obliged to calibrate the data with a reference target and to develop a specific post-processing procedure to compensate for the drift errors [13]. All the data presented here have been calibrated and 'cleaned' using the following procedure.

The post-processing method performed on the scattered field consists of two steps. First, the scattered field is corrected for drift errors. The drift correction was obtained with a minimum bandwidth optimization (see section 3.1 for a description of the principle and [13]). Second, the scattered field is calibrated (via a single complex coefficient at each frequency). The entire data processing procedure used is also described in [15]. Note that the raw data are also available in the data file via the incident field and total field. The raw incident field and total field can also be used as noisy data (without performing any drift correction).

3.1. Drift corrections

When measuring the scattered field in two steps, as we did throughout the Fresnel Database, the main difficulty encountered with low scatterers is the low level of the signal of interest in comparison with the measured field level. Any variations between our two measurements therefore completely disrupted the scattered field. Using the *a priori* information that the

scattered field has to have a limited spectral bandwidth [12], and since this drift can be modeled using a single complex coefficient, we minimize the spectrum of the following quantity: $E_{\text{scat}}^{\text{cor}} = \alpha E_{\text{tot}} - E_{\text{inc}}$ (see [13] for further details), trying to find the most suitable α in order to lower the spectral content of the scattered field.

The best drift coefficient α^* is obtained by minimizing the spectral bandwidth of the scattered field,

$$B(\alpha^*) = \min_{\alpha} \frac{\int \kappa_r^2 \left|\hat{E}_{s,\theta\theta}^{\text{cor}}(\kappa_r)\right|^2 \mathrm{d}\kappa_r}{\int \left|\hat{E}_{s,\theta\theta}^{\text{cor}}(\kappa_r)\right|^2 \mathrm{d}\kappa_r} \tag{1}$$

where $\hat{E}_{s,\theta\theta}^{\text{cor}}$ denotes the Fourier transform along ϕ_r of the corrected scattered field and κ_r is the associated Fourier coordinate. Assuming that when we are dealing only with a given target orientation and a given source location, the drift is either constant or shows negligible variations during the movement of the receiver, the α coefficients are computed for each source and each target orientation. The typical values obtained for α with this minimization procedure have an amplitude of a few tenths of a percent and a phase of a few hundredths of a radian. This really small adjustment can nevertheless lead to quite large corrections.

3.2. Calibration

To be able to perform quantitative inversion procedures, i.e. reconstructions where the shape of the target is not the only information extracted but the dielectric characteristics are also of interest, quantitative values of the fields are required and an accurate calibration procedure therefore has to be applied. The very raw calibration procedure previously adopted with the two-dimensional targets consisted in comparing the measured and simulated incident fields on the receiver located opposite the source. This very simple calibration method was not suitable with the current configuration and did not yield satisfactory results. When dealing with 3D targets, a reference target is therefore required to be able to perform calibrations by comparing the scattered fields instead of the incident ones. Two main difficulties arose when using this procedure, as the reference target has to be very accurately characterized. It is obviously necessary to have a good knowledge of the geometrical and dielectric characteristics of the reference target, but it also has to be accurately positioned in the anechoic chamber. This led us to choose a single metallic (stainless steel) sphere as a reference target because we can also take advantage of its diverging mirror properties. The positioning accuracy of this target can be said to have been ± 0.1 mm in the (xOy) plane and ± 0.5 mm along the Oz-axis [15]. Another interesting property of metals in the microwave range is the fact that metallic targets can be assumed to be perfectly conducting targets.

The calibration method adopted was one of the simplest methods available [17], involving the use of a single 70 mm diameter metallic sphere as a reference target and measuring its scattered field only in the azimuthal plane ((xOy) plane) and in the $\phi\phi$ polarization. The calibration coefficient is computed by comparing the drift-corrected measured field with the simulated field obtained using Mie series and by taking a plane wave excitation of amplitude 1 and phase 0 at the origin of the coordinate system. A single complex 'scaling' coefficient is then obtained at each frequency by minimizing the distance between the measured and simulated scattered fields, and this coefficient is applied to all the measurements (i.e., in the case of each source, receiver and target orientation). The efficiency of this calibration procedure was studied more closely in [9] but it was also possible to use it here because the co- and cross-polarizations were sufficiently isolated (they were typically more than 20 dB apart).

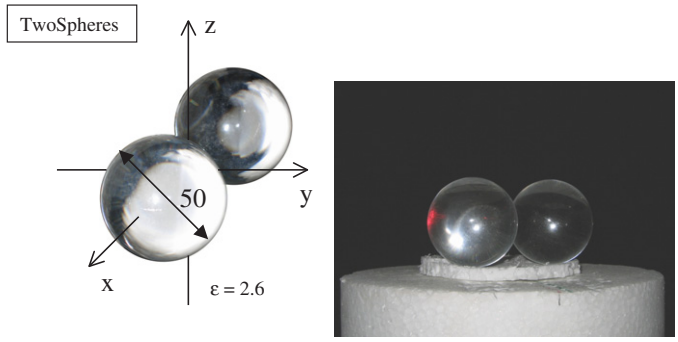

Figure 4. Diagram and picture of the *TwoSpheres* target on the polystyrene mast in the anechoic chamber.

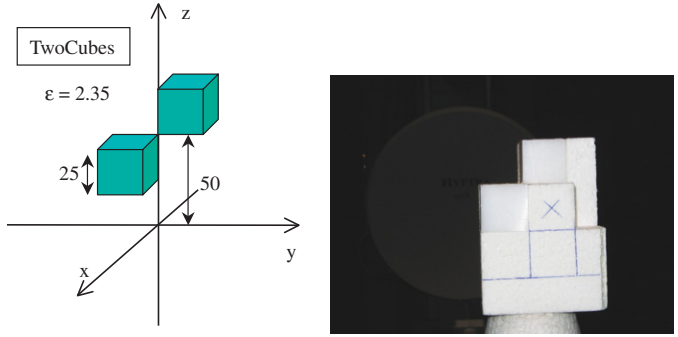

Figure 5. Diagram and picture of the *TwoCubes* target on the polystyrene mast in the anechoic chamber.

4. Targets

The fields scattered by several targets were previously measured and compared with simulated fields, giving good agreement [8, 9, 15]. All the target permittivities have been measured with the commercial kit *EpsiMu* [16]. Scattered fields measured with five different targets are now available in this special section (via the IOP website or our own website at http://www.fresnel.fr/3Ddatabase).

4.1. TwoSpheres

The first target consists of two dielectric spheres 50 mm in diameter with a permittivity of 2.6. Their positions are given by figure 4. One of the difficulties encountered with the inversion may be due to the description of the contact point between the two spheres.

4.2. TwoCubes

The second target consists of two dielectric cubes measuring 25 mm on each side, with a permittivity of 2.3. Their positioning is defined in figure 5. The expanded polystyrene

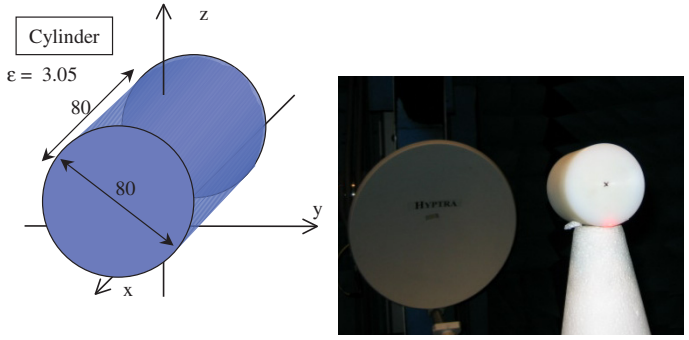

Figure 6. Diagram and picture of the *Cylinder* target on the polystyrene mast in the anechoic chamber.

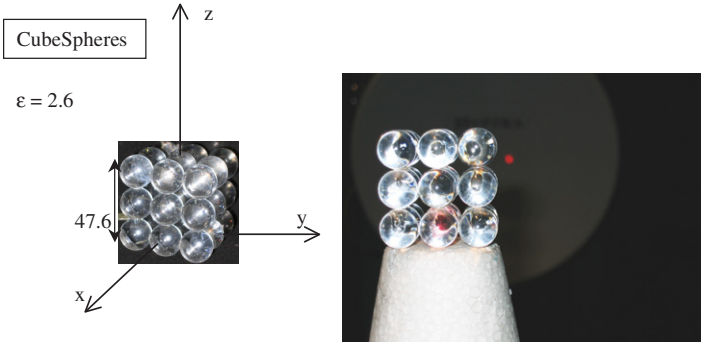

Figure 7. Diagram and picture of the *CubeSpheres* target on the polystyrene mast in the anechoic chamber.

support, which is necessary to maintain the two cubes exactly in place, can be assumed to be perfectly transparent in our frequency range.

4.3. Cylinder

The third target consists of a dielectric cylinder measuring 80 mm side with a diameter of 80 mm and a permittivity of 3.05, and its position is defined in figure 6. Note that this target has the largest volume of all the targets used to draw up the database, and this may cause some difficulties in the case of some inversion algorithms.

4.4. CubeSpheres

The fourth target consists of an aggregate of dielectric spheres. Each sphere has a diameter of 15.9 mm and a permittivity of 2.6. They were assembled so as to obtain a cube measuring 47.6 mm on each side. The positioning of this target is shown in figure 7. Due to the size of the spheres and their arrangement, this target has the finest geometrical details. Scattered field comparisons can be found in [8].

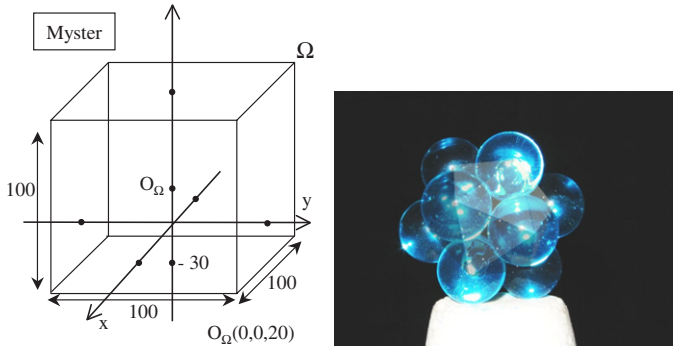

Figure 8. Diagram and picture of the *IsocaSphere* target on the polystyrene mast in the anechoic chamber.

Table 1. Position of the centers of the spheres composing the mystery *IsocaSphere* target.

x (mm)	y (mm)	z (mm)
−6.87	11.90	0.00
−6.87	−11.90	0.00
13.74	0.00	0.00
11.12	19.25	13.74
11.12	−19.25	13.74
−22.23	0.00	13.74
−11.11	−19.25	22.23
22.23	0.00	22.23
−11.12	19.25	22.23
−13.74	0.00	35.97
6.87	11.90	35.97
6.87	−11.90	35.97

4.5. Myster

The fifth target was a mystery target which was enclosed inside a square box measuring 100 mm on each side. In order to obtain a real inverse problem, this target has been kept secret from all the contributors (even those at our laboratory), who had only an approximate idea of its location. The details of the mystery target were only disclosed after the submission of all the papers in this special section

This mystery target, which was renamed *IsocaSphere* (figure 8), is in fact a group of 12 spheres of PMMA ($\varepsilon_r = 2.6$) 23.8 mm in diameter, which were glued together to compose a regular geometrical figure. These spheres were arranged so that their centers lay along the vertices of an icosahedron (see table 1). This was taken to be the optimum position of the 12 sphere centers, assuming the figure to be perfectly implemented and the alignment to be ideal. The transparent isocahedron in the picture has just been added to show the design of this target more clearly. It was positioned in the same way as the *CubeSpheres* target, so that the (xOy) axis crossed the center of the three spheres on which the mystery target lays. The cross-section at $z = 0$ mm should therefore show three circles 23.8 mm in diameter in contact; at $z = 13.74$ mm, three circles with a diameter of 23.8 mm plus three smaller ones (the bottom of the spheres at $z = 22.23$ mm); the same occurs at $z = 22.23$ mm, where the

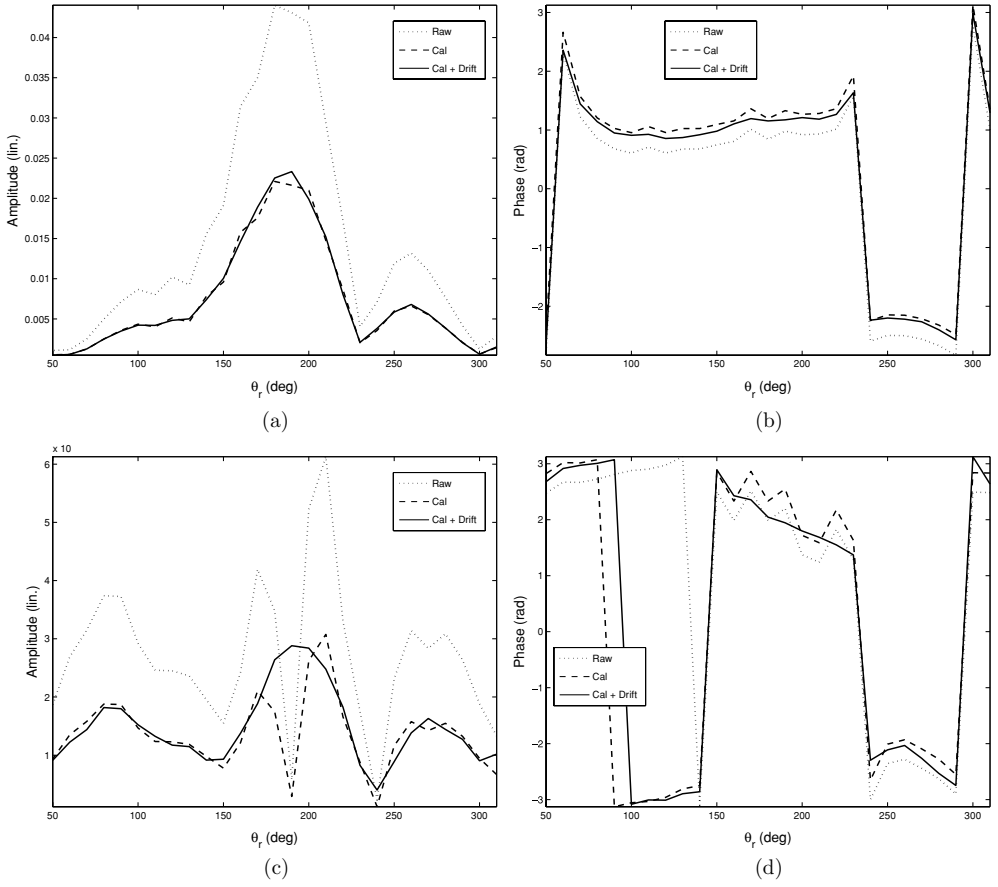

Figure 9. Influence of drift corrections on the field scattered by the *TwoCubes* target, plotted at $\phi_s = 75^\circ$ and at 6 GHz in both polarization cases ($\phi\phi$ and $\theta\phi$). (· · · · · ·) Raw field, (- - - -) calibrated field, (——) calibrated and drift-corrected field. (*a*) Scattered field magnitude ($\phi\phi$); (*b*) scattered field phase ($\phi\phi$); (*c*) scattered field magnitude ($\theta\phi$); (*d*) scattered field phase ($\theta\phi$).

large circle has been replaced by the small ones and vice versa; and at $z = 35.97$ mm, the same figure is obtained as at $z = 0$ but with a rotation of 180°.

5. Files format

There are two files per target, one for each polarization: with extension '_PP.exp' for the $\phi\phi$ polarization and with extension '_TP.exp' for the $\theta\phi$ polarization case. Each file contains the following 10 columns:

θ_s, ϕ_s, θ_r, freq, Re(E_{inc}), Im(E_{inc}), Re(E_{tot}), Im(E_{tot}), Re(E_{scat}), Im(E_{scat})

Re and Im correspond to the real and imaginary parts of the field under consideration. E_{inc} (resp. E_{tot}) is the raw incident (resp. total) field measured at the receiver and E_{scat} is the post-processed scattered field. Any points where saturation of the measured field was encountered were eliminated from the dataset by introducing 0 values instead of the scattered

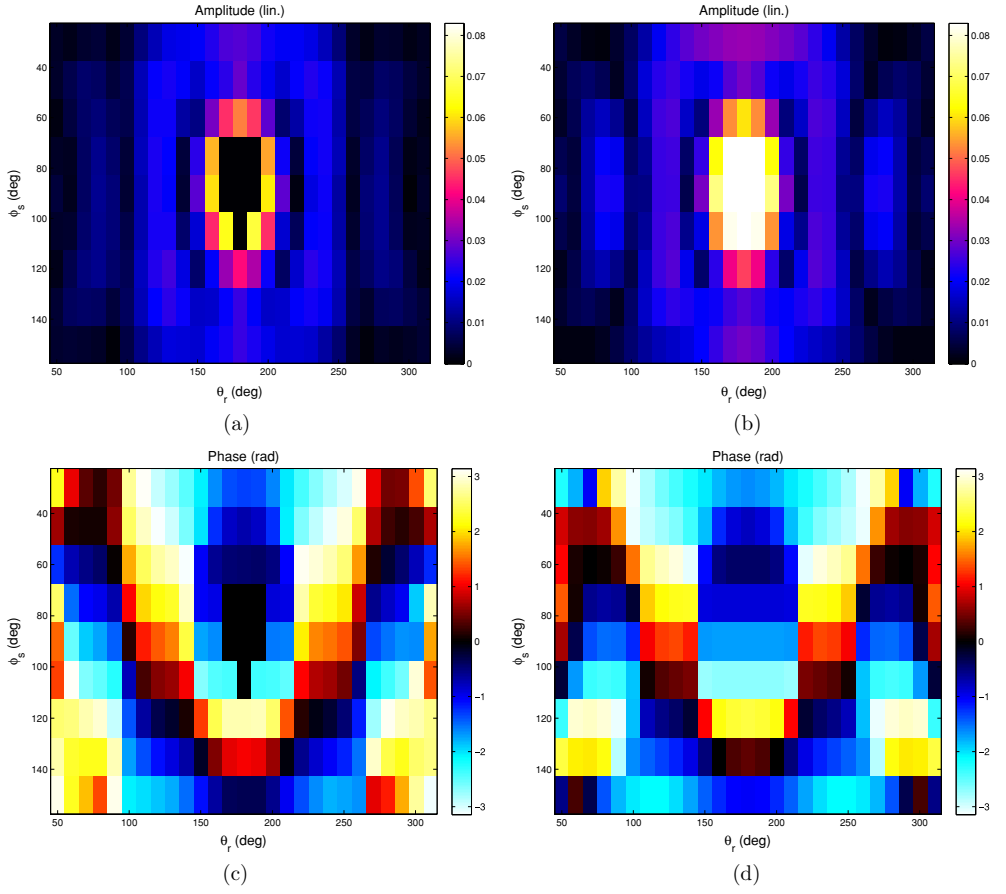

Figure 10. Scattered field obtained with the *Cylinder* target in the $\phi\phi$ polarization, at a single target orientation but with all the source and receiver positions at 4 GHz. (*a*) Measured scattered field magnitude; (*b*) simulated scattered field magnitude; (*c*) measured scattered field phase; (*d*) simulated scattered field phase.

field measurements. This removal of points was performed only on the co-polarized field as the targets are weakly depolarizing targets.

6. Results

6.1. Effects of the drift correction

The drift correction may play an important role, depending on the measurement conditions, as it probably contributes greatly to obtaining satisfactory inversion results. Note that these corrections are of the order of magnitude of the drift that can be observed with the network analyzer itself, and this procedure should be useful with many other configurations. As an example of the effect of these corrections, the raw and post-processed fields obtained with the *TwoCubes* target are presented in figure 9. As can be seen from this figure, the drift correction gives a real smoothing effect, and there is no spectral windowing at all. All the relevant high

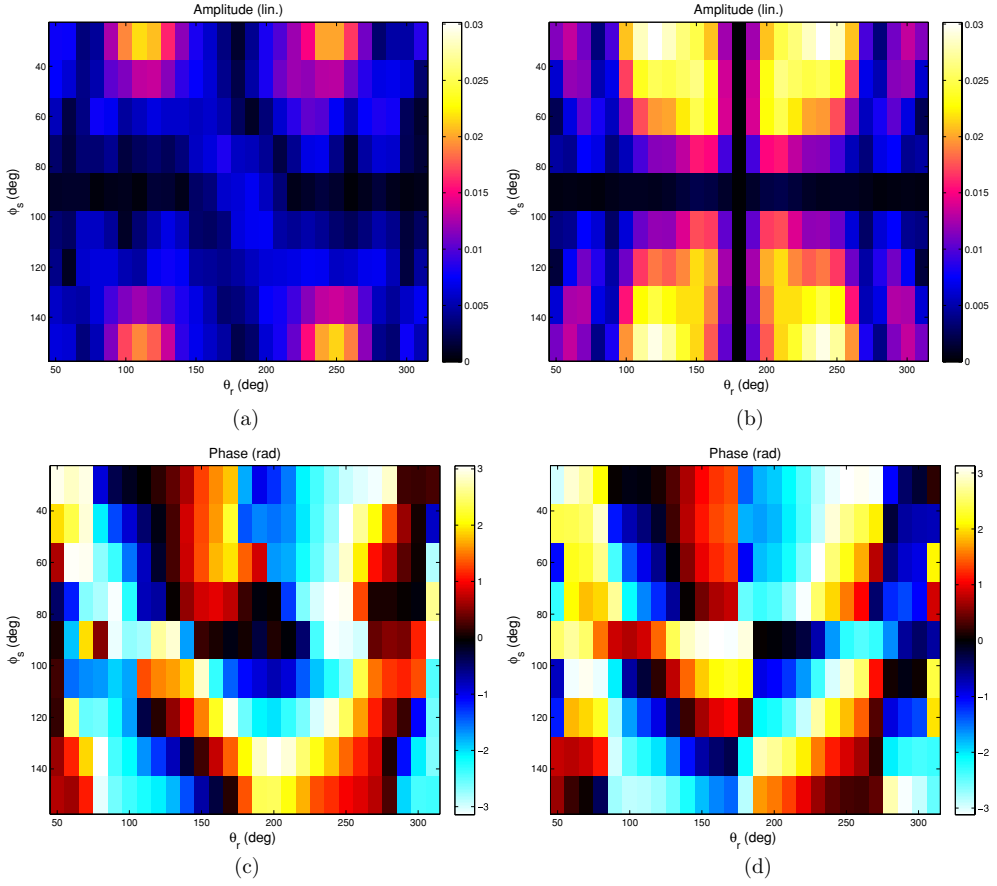

Figure 11. Scattered field obtained with the *Cylinder* target in the $\theta\phi$ polarization, in the case of a single target orientation but with all the source and receiver positions at 4 GHz. (*a*) Measured scattered field magnitude; (*b*) simulated scattered field magnitude; (*c*) measured scattered field phase; (*d*) simulated scattered field phase.

frequencies are therefore kept without any need for any *a priori* information about the target (the only requirement is to perform a sufficient sampling of the scattered field).

6.2. Scattered field comparisons

Detailed comparisons on the scattered field measurements performed with our equipment with several targets can be found in [8, 9] (the *Cylinder* target is also described in [9] and the *CubeSpheres* in [8]). To illustrate the scattered fields measured in this 3D database, two cases are presented here, taking a single target orientation ($\theta_s = 180°$). The fields scattered by the *Cylinder*, the largest target, are presented from figure 10–12 at a frequency of 4 GHz (note that the black areas observed in the center of the plots of the magnitude and phase of the measured $E_{\phi\phi}$ fields are due the removal of the measured points where the mixer was saturated). The simulations were performed using a classical method of moments. To give a more exact idea of how difficult it was to obtain good agreement between the measured and simulated fields, plots of the fields with a given source location are presented in figure 12. In

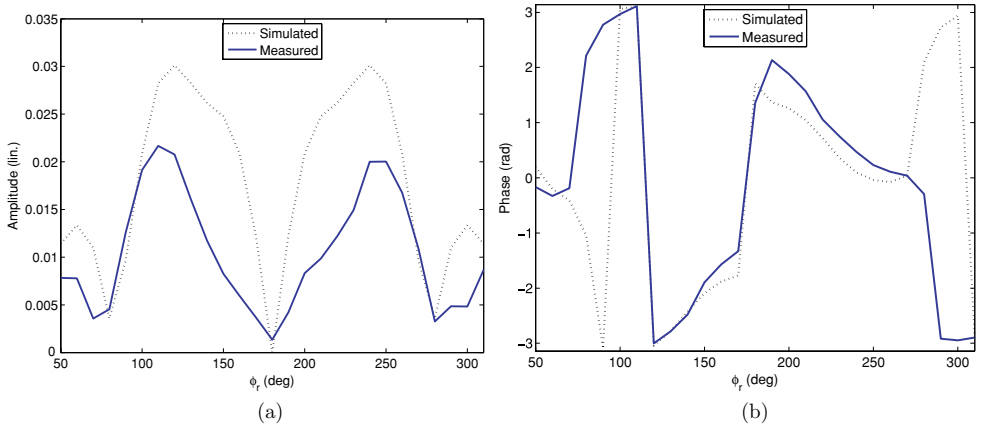

Figure 12. Scattered field obtained with the *Cylinder* target in the $\theta\phi$ polarization, with a single target orientation and, a single source $\theta_s = 30^\circ$ but all the receiver positions at 4 GHz. (*a*) Scattered field magnitudes; (*b*) scattered field phases.

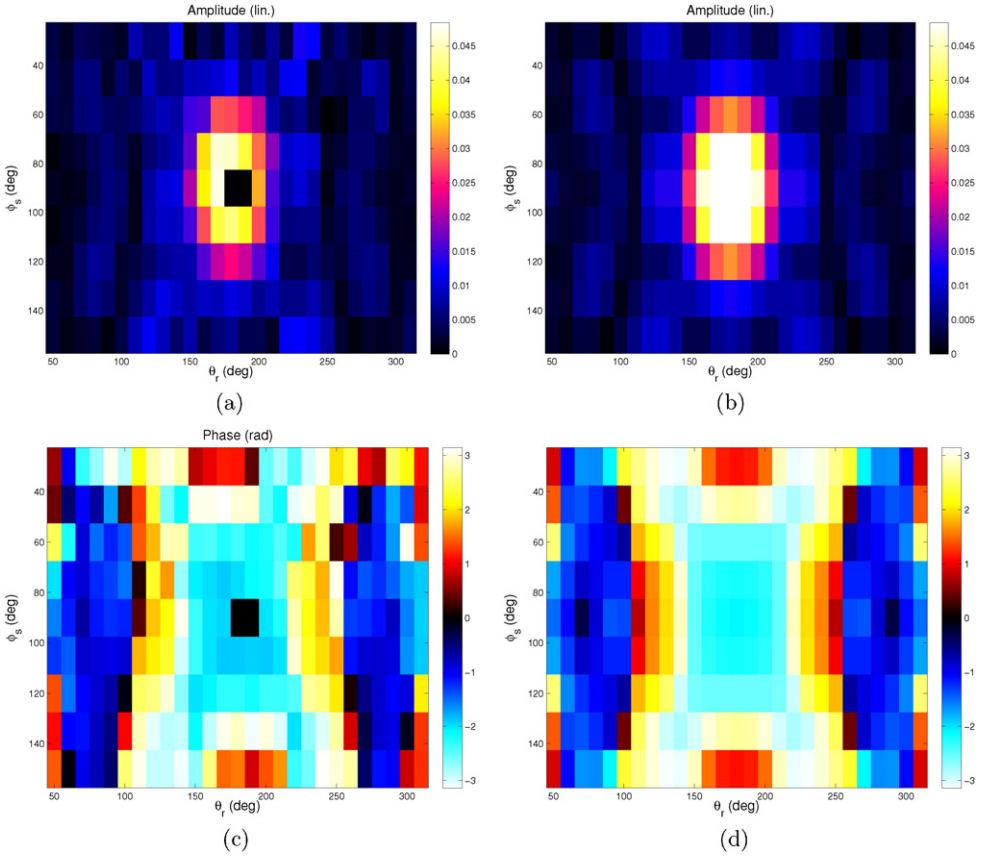

Figure 13. Scattered field obtained with the *TwoSpheres* target in the $\phi\phi$ polarization, with a single target orientation but with all the source and receiver positions at 6 GHz. (*a*) Measured scattered field magnitude; (*b*) simulated scattered field magnitude; (*c*) measured scattered field phase; (*d*) simulated scattered field phase.

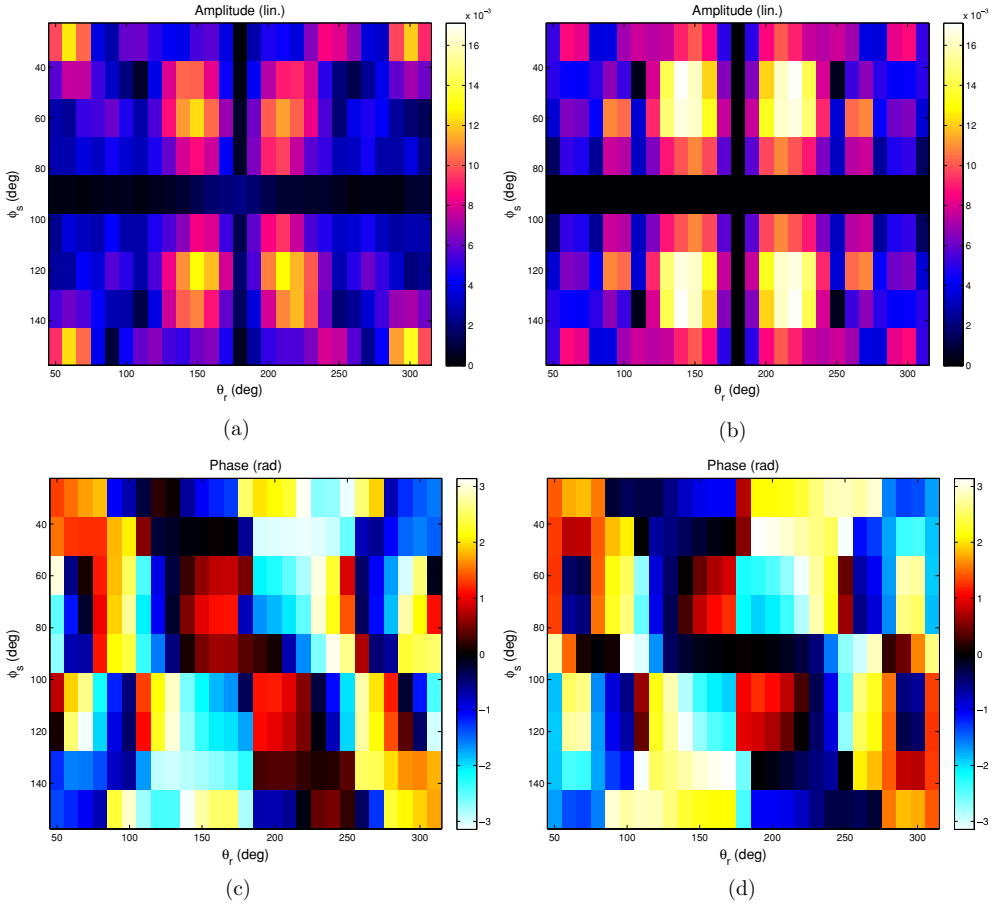

Figure 14. Scattered field obtained with the *TwoSpheres* target in the $\theta\phi$ polarization, with a single target orientation but with all the source and receiver positions at 6 GHz. (*a*) Measured scattered field magnitude; (*b*) simulated scattered field magnitude; (*c*) measured scattered field phase; (*d*) simulated scattered field phase.

fact, the main difficulty involved in the cross polarization measurements results from the very low-measured field levels, which can moreover coincide with low scattered fields. In the case of the *TwoSpheres* target (figures 13 and 14), the simulations were performed with the same code but at 6 GHz. Fairly good agreement was obtained with each source–receiver pair and no special problems were apparently encountered in specific zones such as high elevations. The cross-polarized fields were naturally rather more difficult to obtain accurately, but this was mainly due to the size and the nature of the targets, as they did not have a strongly depolarizing effect. The cross-polarized signal level was therefore very small, sometimes reaching the noise floor level. Note that as the signals measured were very small in the central cross (i.e., when $\theta_r = 180^\circ$ and $\phi_s = 90^\circ$), the phases could be almost impossible to determine at these angular values.

6.3. Error function analysis

Another criterion which can be adopted for comparing the measured and simulated fields is the following error function, this is the cost function which is usually minimized in inversion

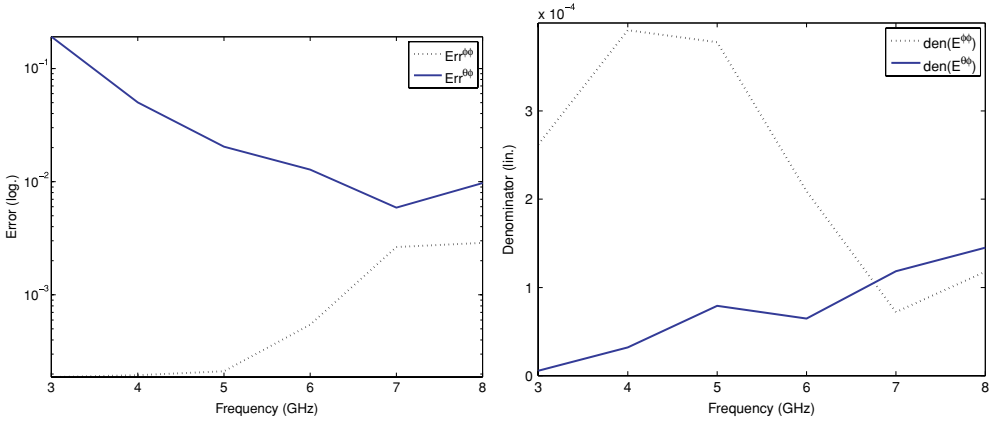

Figure 15. Error function and its denominator in the case of the *TwoSpheres* target in the $\theta\phi$ and $\phi\phi$ polarization states, with a single target orientation but with all the source and receiver positions versus the frequency. (*a*) Error function; (*b*) error function denominator.

algorithms:

$$Err(f) = \frac{1}{N_s N_r} \frac{\sum_{i=1}^{N_s} \sum_{j=1}^{N_r} \left| \mathbf{E_s^{meas}}(\mathbf{r}_i, \mathbf{r}_j, f) - \mathbf{E_s^{sim}}(\mathbf{r}_i, \mathbf{r}_j, f) \right|^2}{\sum_{i=1}^{N_s} \sum_{j=1}^{N_r} \left| \mathbf{E_s^{sim}}(\mathbf{r}_i, \mathbf{r}_j, f) \right|^2}, \tag{2}$$

where $\mathbf{E_s^{sim}}(\mathbf{r}_i, \mathbf{r}_j, f)$ (resp. $\mathbf{E_s^{meas}}(\mathbf{r}_i, \mathbf{r}_j, f)$) denote the simulated (resp. measured) scattered field obtained with the source $\mathbf{r}_i$ and the receiver $\mathbf{r}_j$ at the frequency f. N_r and N_s are the total number of sources and receivers.

The results presented in figure 15 summarize the comparisons between the *TwoSpheres* target measurements and the computations obtained with a classical method of moments with both types of polarization, but with a single target orientation. This criterion also accurately reflects the quality of the measurements, especially in the case of the co-polarization, although some comments need to be made about the cross-polarization.

First, the error in the co-polarization increases in both cases with the frequency, which shows that it is increasingly difficult to make accurate measurements as well as to obtain accurate simulations. Second, the cross polarization error is greater than the co-polarization error at all the frequencies, as was to be expected, but this conclusion should be mitigated by the following comments:

- The measured signals (i.e., the incident and total fields) are very small with this case of polarization at all the frequencies tested.
- As the scattered field is also very low, especially at the lower frequencies, the result of the subtraction between the two measured fields is really sensitive to noise.
- The definition of the error function may have increased the errors at the lower scattered field values simply because the denominator is very small in the case of globally low scattered fields (i.e. scattered fields which have small magnitudes with all the sources and all the receivers. This occurs at the lower frequencies especially in the cross polarization case because the depolarization then becomes very weak (cf figure 15(b)).
- From both the numerical and experimental points of view, the cross-polarization is highly sensitive to errors. In the measurements, any misalignment has dramatic effects, and the discretization errors are also clearly visible in the simulations.

Although further improvements in the experiments would obviously still be worthwhile to improve the cross-polarization measurements (by changing the source antenna, for example, and maybe also by improving the calibration procedure), the error function used in inversion algorithms may also need to be improved to render its behavior more in keeping with the practical experimental issues that we are dealing with here.

7. Conclusion

Adding three-dimensional targets to the Fresnel Database was a really challenging task, and we had to modify our setup and use practically its maximum possibilities at that time. Efforts were also made in terms of the alignment and the calibration, and an original post-processing method had to be developed to meet this specific challenge. The drift correction procedure that has been developed for this purpose will hopefully also be suitable for use with other equipment, as this method can be generalized to other geometries. The analysis of these measurements has suggested some new ideas, and we are already working on methods to increase the sensitivity of the system, using spherical aggregates as well as more complex targets and even smaller ones.

Acknowledgments

We would like to take this opportunity of thanking the organizers of this special section, all the contributors and the people who have helped to make this special section possible, and in particular: Christelle Eyraud (for the direct problem computation and her previous work on drift correction) and Jean-Pierre Spinelli (for all the mechanical aspects).

References

[1] McGahan R V and Kleinman R E 1996 Special session on image reconstruction using real data *IEEE Antennas Propag.* **38** 39–59

[2] McGahan R V and Kleinman R E 1997 Second annual special session on image reconstruction using real data *IEEE Antennas Propag.* **39** 7–32

[3] McGahan R V and Kleinman R E 1999 Third annual special session on image reconstruction using real data: part 1 *IEEE Antennas Propag.* **41** 34–51

[4] McGahan R V and Kleinman R E 1999 Third annual special session on image reconstruction using real data: part 2 *IEEE Antennas Propag.* **41** 20–40

[5] Belkebir K and Saillard M 2001 Special section on testing inversion algorithms against experimental data *Inverse Problems* **17** 1565–71

[6] Belkebir K and Saillard M 2005 Special section on testing inversion algorithms against experimental data: Inhomogeneous targets *Inverse Problems* **21** S1–3

[7] Geffrin J-M, Sabouroux P and Eyraud C 2005 Free space experimental scattering database continuation: experimental set-up and measurement precision *Inverse Problems* **21** S117–30

[8] Sabouroux P, Stout B, Geffrin J-M, Eyraud C, Ayranci I, Vaillon R and Seluk N 2007 Amplitude and phase of light scattered by micro-scale aggregates of dielectric spheres: comparison between theory and microwave analogy experiments *J. Quantum Spectrosc. Radiat. Transfer* **103** 156–67

[9] Eyraud C, Geffrin J-M, Sabouroux P, Chaumet P C, Tortel H, Giovannini H and Litman A 2008 Validation of a 3D bistatic microwave scattering measurement setup *Radio Sci.* **43** RS4018

[10] Hauck B, Ulaby F and DeRoo R 1998 Polarimetric bistatic measurement facility for point and distributed targets *IEEE Trans. Antennas Propag.* **40** 31–40

[11] HP Antenna Guide 1990 Antenna measurement system configuration guide to 45 MHz to 110 GHz (Hewlett-Packard no. 5958-0397)

[12] Bucci O M and Isernia T 1997 Electromagnetic inverse scattering: retrievable information and measurement strategies *Radio Sci.* **32** 2123–37

[13] Eyraud C, Geffrin J-M, Litman A, Sabouroux P and Giovannini H 2006 Drift correction for scattering measurements *Appl. Phys. Lett.* **89** 244104

[14] Geffrin J-M, Chaumet P C, Eyraud C and Belkebir K 2008 Electromagnetic three-dimensional reconstruction of targets from free space experimental data *Appl. Phys. Lett.* **92** 194103

[15] Eyraud C 2006 Caractérisation et optimisation dans le domaine des hyperfréquences des mesures de champs diffractés: applications aux problèmes directs et inverses tridimensionnels *PhD Dissertation* University of Provence, Marseille, France

[16] Sabouroux P and Boschi P 2005 EpsiMu: a new microwave materials measurement kit *Rev. Electr. Electron.* **10** 58–62

[17] van den Berg P M, Coté M G and Kleinman R E 1995 Blind shape reconstruction from experimental data *IEEE Trans. Antennas Propag.* **43** 1389–96